JOURNAL OF GEOPHYSICAL RESEARCH, VOL. 102, NO. D23, PAGES 28,003–28,011, DECEMBER 20, 1997

Earth surface reflectivity climatology at 340–380 nm from TOMS data

J. R. Herman
Laboratory for Atmospheres, NASA Goddard Space Flight Center, Greenbelt, Maryland

E. A. Celarier
Software Corporation of America, Lanham, Maryland

Abstract. The 340–380 nm (UV) Lambertian equivalent reflectivities (LER) of the Earth's surface, between the latitudes ±70°, are constructed from 14.5 years of radiances measured by Nimbus-7/total ozone mapping spectrometer (November 1978 to May 1993). The surface LER values are obtained from the minimum reflectivity values for each 1° × 1.25° (latitude × longitude) pixel with statistically improbable outlier values removed. The resulting LER climatology shows low surface reflectivity values over the entire globe at 340 and 380 nm that are nearly independent of wavelength (the difference is less than 0.2%). In general, the LER is lower over the land (2–4%) than over the oceans (5–8%), though both land and water have features outside of these ranges. Monthly maps of LER are derived that include seasonally persistent cloud features, as well as showing seasonal surface variations. There are low reflectivity regions in the ocean coastal waters that appear to be indicative of chlorophyll or silt from wave action or from rivers. There also are mid-ocean areas of comparatively high reflectivity with a seasonal variation that is not solar zenith angle dependent. These areas of high ocean reflectivity correlate with coastal zone color scanner observations that were associated with the absence of phytoplankton (clear water).

1. Introduction

Nimbus-7/total ozone mapping spectrometer (TOMS) obtained daily measurements of the backscattered radiances from the Earth's atmosphere and surface for the period November 1978 to May 1993. These data cover the entire sunlit portion of the Earth's surface as seen from the near-noon (Sun synchronous) polar orbiting satellite at 950 km altitude. Nimbus-7/TOMS [*Heath et al.*, 1975] measured the amount of backscattered radiance in six 1-nm wide wavelength bands (313, 318, 331, 340, 360, and 380 nm). The TOMS instrument scans perpendicular to its orbital track in a 51° wide swath of 35 scenes to provide contiguous, and sometimes overlapping, coverage of the Earth's surface. The instrumental field-of-view (FOV) dimension on the surface of the Earth is 50 km (about 0.5°) at the nadir position and about 200 km at the largest side scan angle. Each day's data are assembled into a 1° by 1.25° grid (latitude by longitude) by weighted averaging of nearest FOV measurements with the smallest scan angles to produce a value for each grid pixel.

Ozone amounts, Lambertian equivalent reflectivities (LER), surface UV fluxes, SO_2 amounts, and an absorbing aerosol index (indicating tropospheric dust, smoke, and volcanic ash) are derived from the TOMS irradiance data. These have been discussed in previous papers [*Heath et al.*, 1975; *Krueger and Schoeberl*, 1987; *Krueger et al.*, 1995; *Herman et al.*, 1993; *Herman and Larko*, 1994; *Herman et al.*, 1996, 1997; *Hsu et al.*, 1996; *Eck et al.*, 1987; *Eck and Dye*, 1991; *Eck et al.*, 1995]. Although the reflectivities of land and oceans have been investigated in connection with remote sensing of the environment, these studies have generally focused on visible and infrared wavelengths, which are relevant to understanding the radiation budget [*Hendersen-Sellers and Wilson*, 1983a] and to identification of types of cloud, terrain, and vegetation. While about 95% of the solar irradiance is in those spectral regions, ultraviolet radiation is important for the remote sensing of atmospheric chemical constituents (most notably, ozone) and aerosols and a small portion of the total atmospheric energy budget. Recently, it has been shown that UV-absorbing aerosols (smoke, dust, and volcanic ash) can cover about 10% of the Earth's surface with an optical depth of at least 0.1 at 380 nm [*Hsu et al.*, 1996; *Herman et al.*, 1997]. These aerosols affect the atmospheric energy balance in the UV and other wavelength regions and reduce the UV flux striking the surface under aerosol clouds (typically at 3–5 km altitude when not near their source region). The UV region is also important in atmospheric photochemistry (net ozone production, chlorine production from CFCs, etc.). The amount of UV radiation at the surface of the Earth (UV-B, 290–320 nm, and UV-A, 320–400 nm) is of considerable interest [*Tevini*, 1993; *Leffell and Brash*, 1996] because of its impact on biological systems (skin cancer, eye cataracts, plant growth, etc.). The accurate estimation of surface UV and aerosol amounts from satellite data requires a knowledge of the ultraviolet reflectivity of the surface [*Herman et al.*, 1996, 1997; O. Torres et al., Derivation of aerosol properties from satellite measurements of backscattered ultraviolet radiation: Theoretical basis, submitted to *Journal of Geophysical Research*, 1997, hereinafter referred to as Torres et al., submitted manuscript, 1997].

Ground-based measurements of UV albedos of various surfaces have been made, but most of these have tended to be

Paper number 97JD02074.
0148-0227/97/97JD-02074$09.00

broadband measurements in combined UV-visible regions [*Hendersen-Sellers and Wilson*, 1983a, b]. A few UV-spectral measurements have been described in the literature for limited scene types [*McKenzie et al.*, 1996; *Doda and Green*, 1980; *Diffey et al.*, 1995]. TOMS scene reflectivities have been studied [*Eck et al.*, 1987], using a minimum reflectance technique to exclude clouds, sea glint, and rough seas, and these reflectivities were compared to a limited set of aircraft-based measurements [*Doda and Green*, 1980]. Minimum TOMS reflectivities over clear ocean areas were also used to monitor the Nimbus-7/TOMS calibration [*Herman et al.*, 1991].

This paper presents global maps of the Lambertian equivalent surface reflectivity (LER) for each month of the year based on 14.5 years of data (November 1978 to May 1993), and a combined global map, where each pixel is the minimum of the monthly minima. The maps are estimates of the Earth's surface reflectivity in the near ultraviolet (340–380 nm) for the region between $\pm 70°$ latitude. We describe the occurrence of well defined features related to ocean and land surface phenomena, as well as seasonal surface and atmospheric processes, that are visible in the monthly and combined LER maps.

2. Lambertian Equivalent Surface Reflectivity

The TOMS instrument was designed to provide accurate global estimates of total column ozone using three wavelength channels selected for their ozone absorption characteristics (313, 318, and 331 nm) and three nonabsorbing wavelength bands (340, 360, and 380 nm). The three nonabsorbing wavelength channels were intended to test the ability of atmospheric radiative transfer models to reproduce the observed wavelength dependence of the backscattered radiation. Since atmospheric absorption at these longer wavelengths is weak, the backscattered intensity is essentially determined by molecular (Rayleigh) scattering, surface reflectivity, and (Mie) scattering from aerosols and clouds.

Early results from satellite measurements showed that the LER atmospheric model proposed by *Davé* [1978] reproduced the wavelength dependence of the observed radiation under a wide variety of observing conditions. In Davé's LER model the atmosphere consists of Rayleigh scatterers bounded by a surface whose Lambertian equivalent reflectivity R is estimated from the measured radiances [*Bhartia et al.*, 1993]. For a pure Rayleigh atmosphere, R is an estimate of the value of the bidirectional reflectivity distribution function (BRDF; the fraction of flux incident at a given angle reflected into an outgoing angle per steradian [*Lenoble*, 1993]) of the surface at a given measurement geometry. If the true BRDF is anisotropic, R will differ from the BRDF value because of the mixing of reflection angles due to subsequent atmospheric scattering.

In the presence of clouds and aerosols, R is greater than the BRDF of the surface, except when enough UV-absorbing aerosols are present to make the losses due to absorption greater than increases from backscattering. An example of this darkening occurs over most of the Saharan desert when dust is airborne for all months except November. Detailed radiative transfer calculations show that Mie scattering can also make R spectrally dependent. This effect is most pronounced for UV-absorbing aerosols, which cause R to decrease with decreasing wavelength [*Hsu et al.*, 1996; *Herman et al.*, 1997]. Nonabsorbing aerosols and low altitude clouds, under certain conditions, can cause R to increase with decreasing wavelength. Under most conditions, however, the TOMS data reveal that R(340 nm) is equal to R(380 nm), within the measurement uncertainty, $\Delta R = \pm 0.2\%$. Typical values of R are 2–4% for land and 5–8% for ocean, 50% for clouds, and 90–100% for clean snow and ice.

TOMS measured both radiance and solar irradiance (using a diffuser plate) with the same instrument to determine initial radiance-irradiance ratios. For the remainder of the TOMS mission it was assumed that the solar irradiance remained constant for the 340–380 nm wavelength range, based on *Schlesinger and Cebula* [1992]. Absolute calibrations for each reflectivity wavelength channel (331, 340, 360, and 380 nm) were made using the differential sensitivity to calibration errors of each pair of wavelengths [*Wellemeyer et al.*, 1996]. Errors in absolute calibration using the "spectral discrimination method" were estimated to be less than 1% per decade. Values of minimum sea surface reflectivity and ice reflectivity in Antarctica and Greenland, used to validate the throughput of the spectrometer over the lifetime of TOMS, showed agreement to 2% in radiance and 1% in derived reflectivity [*Wellemeyer et al.*, 1996]. A similar analysis of ice radiances and reflectivities to validate the spectral discrimination method is described for Meteor-3/TOMS [*Jaross et al.*, 1995].

3. Minimum Lambertian Surface Reflectivity

The quantity of interest in the remainder of this paper is the closest approximation to the 340 and 380 nm (LER) reflectivities R of the Earth's surface available from TOMS backscattered radiance data. For this purpose, the TOMS backscattered radiances are calculated using the form of the radiative transfer solution suggested by Davé [1978], where R is determined by requiring that the measured radiance from TOMS equal the calculated radiance at 340 or 380 nm.

In general, R is affected by the presence of clouds, haze, and aerosols in each instrumental field-of-view (FOV) unless the scene is clear. Even for the clearest of midday scenes, when Nimbus-7/TOMS measurements were made, the Earth's surface is frequently covered by a thin, low-lying surface haze whose scattering can slightly increase R and also make the apparent BRDF, measured from space, slightly more isotropic by diffusing the reflected light. When daily ozone amounts are estimated from the TOMS radiances, the daily R values may be haze-enhanced. This causes no significant error in ozone determination, since the haze lies under almost all of the atmosphere and ozone column. Because we use minimum R values in this study, contamination by ground haze should be minimized and should closely represent the LER of the Earth's surface (land, foliage, and water). Marine aerosols and water haze over land cause a small brightening of the apparent surface reflectivity. The mean brightening appears to be of the order of 1% with a narrow distribution of values about the mean.

The objective quantities of the present study are the minimum LERs in the processed $1° \times 1.25°$ gridded LER values obtained from 14.5 years of Nimbus-7/TOMS data. Minimum reflectivities were determined for each month of the year as well as over the entire data record. The resulting data set has a preponderance of values tightly clustered about R values of a few percent and a small set of statistically improbable outlier points. Outlier points caused by noise in the system or unusual atmospheric conditions were removed. Examples of such points are the rare values of negative reflectivities and one or two isolated points of extremely low reflectivity separated from the main body of the data as shown in Figure 1.

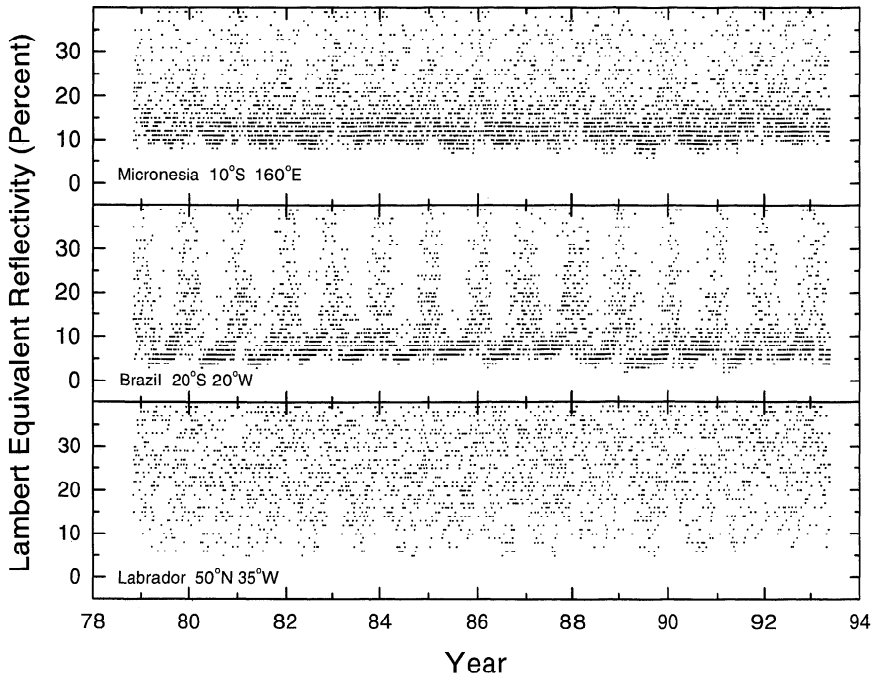

Figure 1. Time series of daily reflectivities at three ocean sites: tropical South Atlantic Ocean, off the coast of Brazil; tropical Pacific Ocean, in the region of Micronesia; and a location over the Great Banks off the Labrador Coast, in the North Atlantic. The lower "envelope" of points is used to define the monthly minimum reflectivities.

The reflectivity data were read from the Version-7 Nimbus-7/TOMS record for all measurements made within each month of the year. The Version-7 reflectivities include a modification for partial cloud coverage whenever the reflectivity is greater than 8%. Because of this, larger values of the Version-7 reflectivities do not represent ground LERs, but rather a weighted average of ground and cloud reflectivity that gradually deviates from the surface LER as the reflectivity increases. This does not affect the present calculations, since most of the cloud-free surface reflectivities in the wavelength range from 340–380 nm are less than 8%.

To find the minimum reflectivities for each $1° \times 1.25°$ pixel, the following procedure is used. Approximately 400 values for each pixel were assembled into monthly histograms after rejecting the infrequently found small negative values. The smallest R values found for each pixel usually differ by at most 2%. In such cases, if the frequency of occurrence of the smallest value is at least half that of the second-smallest value, the smallest value is used. If the two smallest values are separated by less than 2%, but the frequency of occurrence of the smallest is less than half that of the second smallest, then the frequency-weighted average of these two values is used. If the separation between the smallest and second-smallest values is at least 2%, then the smallest is used only if its frequency of occurrence exceeds 3/4 that of the second smallest. In those few cases where this condition was not met (mostly at very high latitudes), the value at a particular pixel was obtained by distance-weighted interpolation within the 5-pixel by 5-pixel neighborhood of the pixel in question. The above procedure results in the selection of the measured minimum value whenever its frequency of occurrence indicates that it is representative of the pixel and not an artifact of the LER determination. It also results in rejection of outlier values that are not statistically representative of the pixel.

The relative accuracies of the measured TOMS radiances are about $\pm 0.1\%$ in the stored high spatial-resolution orbital data set, and their absolute accuracy was maintained to better than 1% per decade [*Herman et al.*, 1991; *Wellemeyer et al.*, 1996]. However, for the purposes of this study, the much smaller $1° \times 1.25°$ gridded data set is used for producing reflectivity maps. These have the same accuracy, but are stored as three-digit numbers and so have a resolution of 1%.

Figure 1 shows examples of actual time series of daily reflectivities (November 1978 to May 1993) at three ocean locations for the entire Nimbus-7/TOMS data record, from which the LERs have been calculated. The locations are in the tropical South Atlantic Ocean, off the coast of Brazil, in the tropical Pacific Ocean, in the region of Micronesia, and at a location over the Great Banks off the Labrador Coast in the North Atlantic. Each time series is from a pixel within a region where there is substantial month-to-month variability in the LER. The monthly LER (MLER) represents the envelope at the bottom of these point scatters, binned by month. While there is considerable scatter in the daily reflectivities, the lower edge of the scatter is quite sharply defined for the two tropical cases shown. In the North Atlantic case the lower edge is much less well defined. The ill-defined scatter in the lower edge may be associated with pervasive late-morning sea fogs since the TOMS measurements were made between 1030 LT (1993) and near-noon (1979). Accumulation of monthly data over the entire 14.5-year period gives a much more well-defined seasonal variation in the monthly minima for this location.

The resulting 380 nm minimum LER maps are shown in the following figures. Plate 1 shows the estimated surface LER (ESLER) determined from every day's data for the 14.5 years. In this Plate, features caused by seasonally persistent clouds, seasonal snow and ice coverage, and seasonal aerosol plumes are not present. Except in the presence of certain kinds of

desert dust, minimum reflectivity maps created from the orbital data set for the difference $R(340) - R(380)$ show that values of $R(340)$ are within 0.2% of $R(380)$. Plates 2–5 show four monthly LER (MLER) climatological maps determined from all data from within each month over the 14.5 years. Seasonal variations in the LER data represent changes in the oceans between nearly clear water and water containing pigmented organisms or silt, land-surface changes in foliage or aridity, as well as seasonally persistent clouds, snow, ice, and aerosol features.

When typical absorbing aerosols with small particle size are present in the atmosphere (e.g., smoke plumes), the reflectivities for both 340 and 380 nm increase by slightly different amounts. Larger particle sizes (e.g., desert dust plumes with smaller single scattering albedos ω than smoke) cause the reflectivities for both 340 and 380 nm to decrease by slightly different amounts. This change in contrast is the basis for the detection of absorbing aerosols over both land and water [*Herman et al.*, 1997; *Hsu et al.*, 1996]. The reflectivity changes caused by smoke and dust are approximately 3–4%.

The seasonally varying absorbing aerosol features cause the apparent surface reflectivities (3–4%) over the Sahara desert to appear lower than those of the true surface (6–8%). For large particle sizes typical of desert dust, the single scattering coalbedo is much larger than for the smaller particle sizes typical of smoke. A model calculation using parameters appropriate for desert dust plumes shows that the measured reflectivity is lower than the underlying surface reflectivity whenever the single scattering coalbedo $(1 - \omega)$ is sufficiently large, in this case 0.16 or larger. Note: the single scattering coalbedo is the ratio of the extinction coefficient for absorption to the total extinction coefficient, absorption plus scattering. Cases where the dust may be composed of finer particles would produce higher reflectivities than the underlying surface. These higher reflectivity data would be screened out of the minimum LER values in Plates 1–5 whenever there is a clear-sky day within the covered time interval.

While smoke and dust have similar absorption refractive indices, the smaller particle size for smoke gives rise to a smaller value of $1 - \omega$. The result is that smoke tends to increase the apparent reflectivity of a scene, while the larger particles of Saharan dust mostly decreases the reflectivity. An example of the higher 8% surface LER is seen within the Libyan desert in the ESLER (Plate 1) and in the MLER (Plates 2–5). The higher surface LER is also seen in many areas of the Sahara in the MLER, especially during the month of November when the amount of desert dust in the air is at its annual minimum.

In the single-channel reflectivity data, smoke tends to be indistinguishable from a thin cloud both in the UV and visible regions of the spectrum. In both cases it brightens the scene relative to the dark background vegetation. These can be seen in the images presented by *Hsu et al.*, [1996, Plate 1 and Figure 1] as part of a discussion of biomass burning in South America. In the visible GOES-7 satellite image the biomass burning smoke appears as a white plume over a dark background. In the TOMS 380 nm channel data the smoke appears as regions of 10–20% reflectivity over a darker 4% reflectivity background. Also shown are thin water clouds appearing as regions of 20–30% reflectivity and dense clouds of 80–90% reflectivity that appear in both the TOMS and GOES-7 data for August 18, 1987.

As shown in Plate 1, the most frequently occurring ESLER values are lower over the land (2–4%) than over the oceans (4–7%), with values in these ranges present over at least 90% of their respective regions. Over land, prominent features with greater LER are associated with permanent glaciers (e.g., the Himalayas-Hindu Kush-Tian Shan region, the Rocky Mountains-Alaska Range, and the Andes, as well as the Greenland ice sheet) and with high desert (e.g., the Libyan desert) and regions with large dry-lake and dry-stream beds (e.g., Lake Eyre, in south central Australia, and the Tibetan Plateau). The higher-reflectivity regions in Africa north of the equator also coincide with the sources of much of the desert dust seen blowing across Africa and the Atlantic Ocean [*Herman et al.*, 1997]. Relatively low reflectivities (0–2%) over land tend to be associated with moderate-elevation, vegetated regions, for example, the Pampas of Argentina and the central African highlands of southern Zaire and northern Zambia, eastern South Africa, and the western foothills of the Great Dividing Range of Australia. Such low reflectivities may be due to absorption at 380 nm by chlorophyll-a and carotenoids in the vegetation. Reflectivity values of up to 2% are consistent with direct spectral measurements of the albedos of grass- and clover-covered surfaces [*McKenzie et al.*, 1996].

For most of the ocean area the ESLER tends to be in two ranges, 5–6% and 4–5%, in well defined regions. In addition, there are small regions of higher ESLER that are 6–7%, and isolated regions of 7–8%. Some coastal waters have lower LERs than the surrounding waters (2–3%, compared to 4–5%). Some such cases appear to be shelf waters; for instance, the Falklands Shelf, the Great Banks off the coast of Newfoundland, the Arafura and Timor Seas north and northwest of Australia. In other cases, such as the waters off the west coasts of North and South America and the west coast of subequatorial Africa, it is less clear that the smaller LERs are associated with ocean floor topography. In such regions they may be due to permanent phytoplankton blooms, ocean dynamic effects on silt suspension, intense wave action, or absorbing-aerosol deposition on the ocean surface. Low reflectivity plumes seen near the mouths of large rivers, such as the Amazon and Congo, may reflect drainage of silt containing various types of organic material, including humic and fulvic acids [*Bukata et al.*, 1995; *Shifrin*, 1988]. The MLER maps show a definite seasonal variation in the LERs of these coastal waters. In some regions, notably the shelf regions, and the west coast of North and South America and the west and southwest coasts of subequatorial Africa, the monthly variations in low reflectivities appear to correlate with monthly variations in high chlorophyll concentration, as determined from the coastal zone color scanner (CZCS) (October 1978 to June 1986) data [*Hovis et al.*, 1980; *Esaias et al.*, 1986].

4. Monthly Data

The MLER maps for January, April, July, and October are presented in Plates 2–5. The MLER is mostly representative of the seasonally varying surface LER, but there are also features that are attributable to time-dependent atmospheric and snow/ice effects. Some care must be taken in the interpretation of the monthly maps when used as surface reflectivity climatologies in radiative transfer calculations. For this purpose, it may be necessary to replace values that are clearly due to atmospheric phenomena (e.g., clouds) with known surface values obtained from the ESLER values of the pixels in question. The remainder of this section is a discussion of some of the more prominent features seen in the MLER maps (see Plates 2–5).

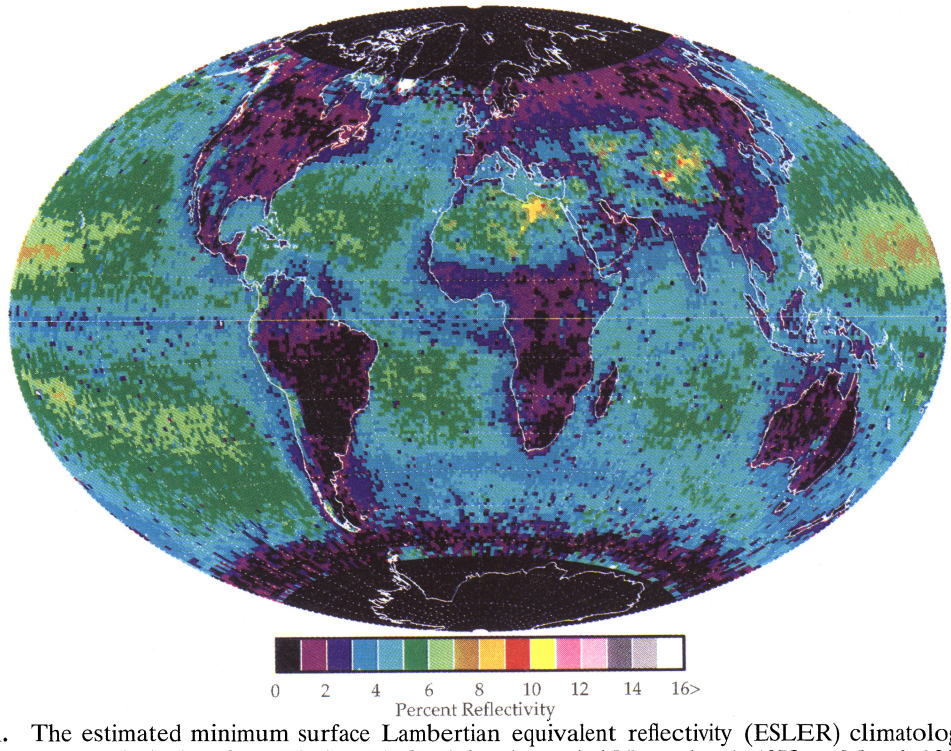

Plate 1. The estimated minimum surface Lambertian equivalent reflectivity (ESLER) climatology determined from every day's data from Nimbus-7/TOMS for the period November 1, 1978, to May 6, 1993, in the latitude band ±70°. In general, the ESLER is lower over the land (2–4%) than over the oceans (5–7%), though both land and water have features outside of these ranges.

The seasonal advance and retreat of snow cover over land in the northern hemisphere is readily apparent in Plates 2–5. Since the color scale used does not differentiate between LERs greater than 15%, broken patches of snow cover are indistinguishable from complete snow cover in these maps. Because we do not attempt to distinguish snow from cloud cover, the LERs may overestimate or underestimate the surface reflectivity when there is complete or partial cloud cover over a snow-covered landscape. Seasonal variations in snow cover on major mountain ranges are easily seen as patches of high-value LER; the Rocky Mountains, the Alps, the Caucasus, the Hindu Kush, and Tian Shan ranges are clearly seen in January's map. Since there is far less land in the high southern latitudes, this effect is not seen as prominently in the southern hemisphere winter (July and October maps); however, one sees some encroachment of the Antarctic ice pack into latitudes near 70°S in the winter months.

In the tropics the R values of land areas are nearly constant through the year, except for desert regions and regions affected by seasonal, persistent cloud cover. The northeast coast of South America, for example, is affected in January–April by sea breeze clouds, as is the region along the Gulf of Guinea in July–October. In June the R values show the western monsoon cyclone over the Arabian Sea, followed by a persistent cloud cover that moves ashore over Gujarat State on the west coast of India (see the July map in Plate 4). A seasonal cycle in the LER over the Arabian desert and the Sahara desert is readily discerned. The seasonal winds in the Sahara and Sahel regions loft great amounts of desert dust that are carried westward across the Atlantic Ocean. The desert dust is an absorbing aerosol that tends to differentially decrease the backscattered 340 and 380 nm radiances seen by TOMS [*Herman et al.*, 1997]. Another interesting feature is the Lake Eyre region in south central Australia. This is a semidry lake bed that is mostly below sea level. There is a seasonal pattern in the size and MLER of the region seen in the maps, tending to be larger in the southern hemisphere summer than in the winter. This follows the known wet-dry cycle for the Lake Eyre region; in the summer it is dry and subject to alluviation that gives rise to a greater LER and to airborne dust (both seen by TOMS), while in the winter it is wet and less reflective.

As indicated above, in the ESLER, most of the ocean area is cleanly divided into two regions, with the respective ranges, 5–6% and 4–5%. In the rest of the ocean there are small regions where the ESLER is higher, about 6–7%, and isolated regions where it attains values of 7–8%. Examination of the MLER maps shows that in the small regions the MLER varies cyclically over the year, with MLERs as high as 9%, and that the boundaries of these regions do not move latitudinally with the seasons. This implies that the higher reflectivity regions are associated with the ocean itself and not with solar zenith angle effects on TOMS observations. The observed high LER regions are associated with areas that are known to be plankton-free for most of the year (e.g., the Sargasso sea, a gyre region in the ocean whose water is quite isolated from the surrounding area), so that the higher ocean reflectivities are associated with clear water. The low reflectivity areas observed in many parts of the oceans and coastal regions are known to contain large amounts of phytoplankton (e.g., the region off the coast of South Africa).

The spatial and temporal variations of the higher ocean LER features correlate well with the lowest chlorophyll concentration features, as measured in the visible region of the spectrum in data from the CZCS, also aboard the Nimbus-7 spacecraft [*McClain et al.*, 1993]. Light-harvesting complexes in many phytoplankton species have nearly as strong an absorption (in vivo) at 380 nm as they do around 400–420 nm in one

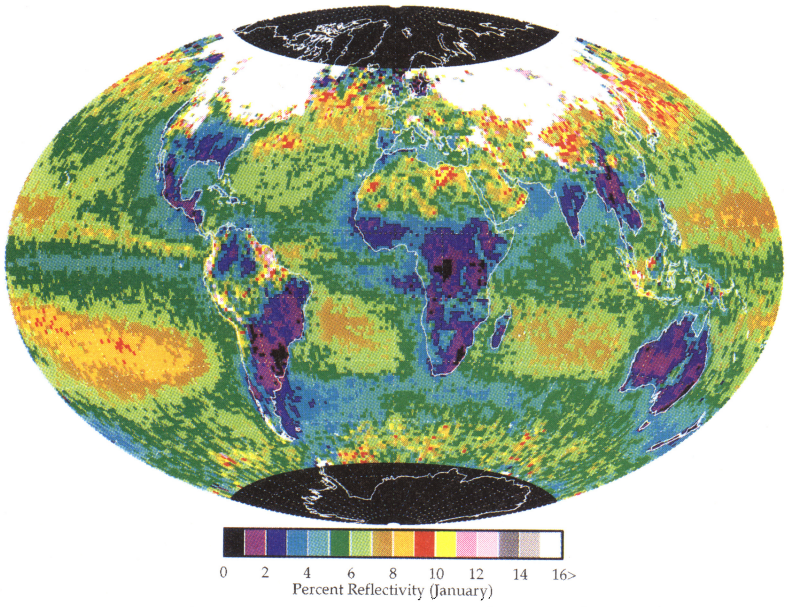

Plate 2. The monthly values of the Lambertian equivalent reflectivity (MLER) for January, obtained from 14.5 years of TOMS 380 nm LER data. Persistent atmospheric phenomena and surface features (snow and ice) appear in the monthly maps.

of the spectral ranges used to determine ocean chlorophyll content [*Morel and Bricaud*, 1981]. When the high reflectivity features in earlier months of the year become smaller and less reflective, it may be due to the incursion of phytoplankton into these regions from regions of intense primary production. Clear water LERs in excess of 8% are consistent with calculations by *Gordon and Jacobs* [1977] of 8.2% at a solar zenith angle of 0°. They also calculate the albedo of clear ocean water at a solar zenith angle of 60° to be 16.9%. However, the LERs determined from TOMS irradiances do not show such high values at 60° solar zenith angle.

A persistent feature seen throughout the year is a relatively low (3–5%) reflectivity in a very narrow band between the equator and 5°N in the Pacific Ocean. This may be due to plankton produced off the west coast of South America as it is entrained by the south equatorial current and concentrated near the surface by upwelling in this region. North of this in the Atlantic and eastern Pacific oceans during the northern hemisphere winter (evident in the October and January maps, Plates 4 and 2), there is a pronounced narrow band where the reflectivity is relatively high (9–10%), lying between 5°N and 10°N. Since this feature is most prominent during times when the North Pacific reflectivity is greatest, it may be due to the eastward transport of clear water from the tropical North Pacific by the equatorial counter current. The fact that its location does not move seasonally in a north-south direction suggests that this band is not a cloud feature associated with the intertropical convergence zone (ITCZ).

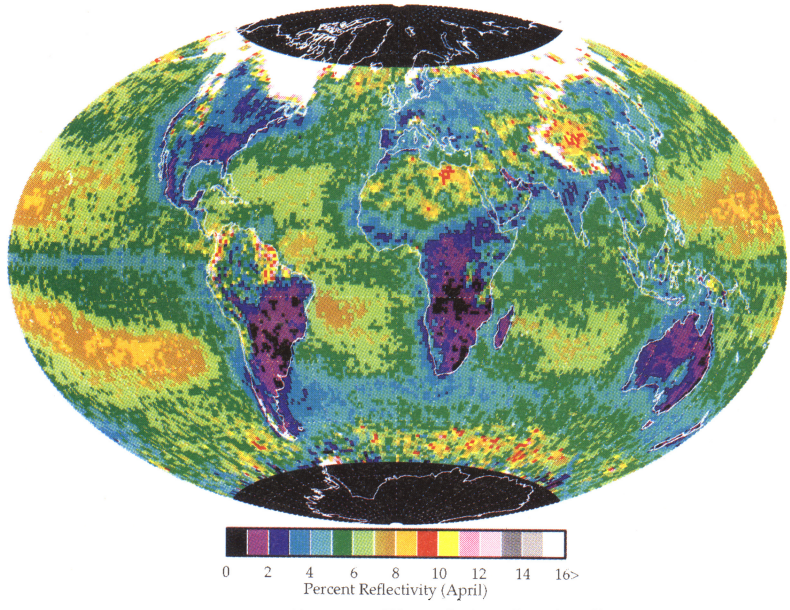

Plate 3. Same as Plate 2, but for April.

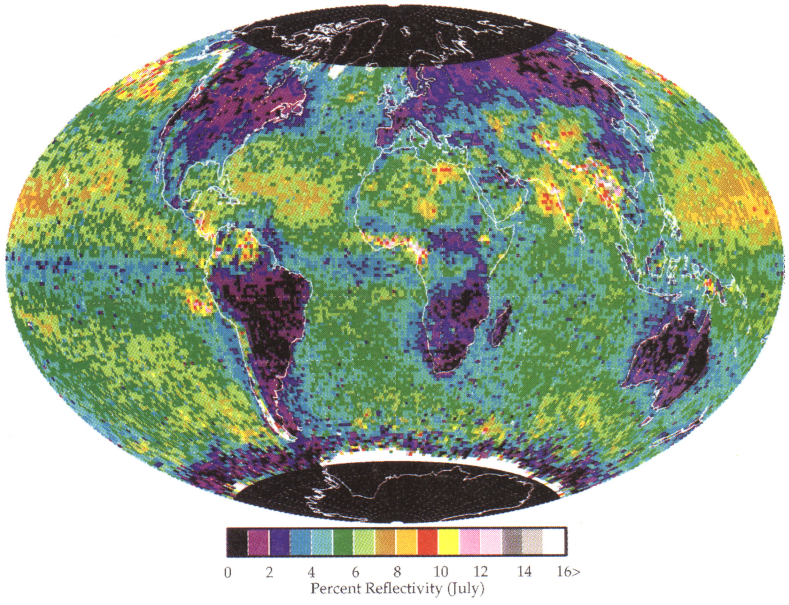

Plate 4. Same as Plate 2, but for July.

Above 50°N in the North Atlantic and North Pacific the reflectivity is low (mostly around 4–6%) from May through September. It increases in October, with a high-reflectivity region (up to 13–14%) that spreads over a larger region through December, then shrinks from January through May. This phenomenon may be attributed to late-morning fogs over the oceans during these months and in part to foamy sea surfaces that tend to be somewhat more reflective in the visible and ultraviolet. Since the increase in reflectivity is seen as early as October, it is unlikely that the reflectivity increase is due in large part to sea ice, though ice may contribute in the late winter and early spring reflectivities.

In the Antarctic Ocean, south of 50°, the reflectivity field is characterized by large pixel-to-pixel variation in every month. There is some seasonal variation in addition to the spatial variation. These seas are very rough throughout the year, and this may give rise to enhanced reflectivity due to foam and whitecaps [*Gordon and Jacobs*, 1977]. Unlike the northern oceans, there is little incursion of warm currents into the Antarctic Ocean, so one does not expect as great a seasonal variation due to fog over the southern as over the northern oceans. In addition to the water surface reflectivity features, one sees the incursion of the Antarctic ice sheet into the region in the southern hemisphere winter (see July and October maps, Plates 4 and 5).

5. Conclusions

The 340 and 380 nm estimated surface Lambertian equivalent reflectivities (ESLER) for the Earth's surface have been calculated from measured Nimbus-7/total ozone mapping spectrometer (TOMS) radiances (November 1978 to May

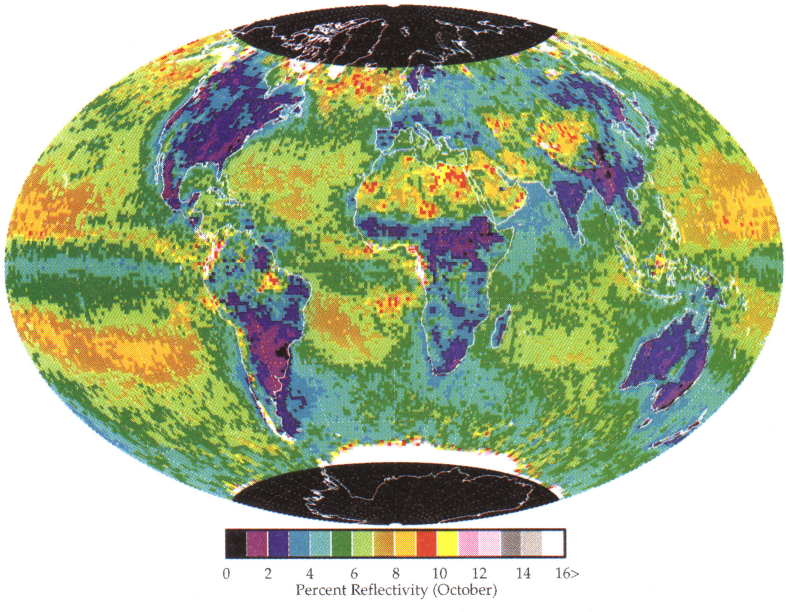

Plate 5. Same as Plate 2, but for October.

1993). The ESLER values are obtained from the 14.5 year minimum reflectivity values for each 1° × 1.25° (latitude × longitude) pixel, with outlier values removed. The resulting ESLER climatology shows low reflectivity values over the entire globe at 340 and 380 nm. In general, the ESLER is lower over the land (2–4%) than over the oceans (5–7%), though both land and water have features outside of these ranges. Within the absolute accuracy of the TOMS reflectivity measurements, $\Delta R = \pm 0.1\%$, the reflectivities at 340 nm equal those at 380 nm, except in the presence of absorbing aerosols and certain low altitude nonabsorbing aerosols. Water clouds do not appear in the R(380 nm) − R(340 nm) reflectivity differences or in the reflectivity residues [*Hsu et al.*, 1996; *Herman et al.*, 1997].

Monthly values of reflectivity are shown that retain the persistent cloud and surface features as well as showing seasonal variation of the surface itself. There are features seen in the ocean coastal waters, indicative of silt from wave action or from rivers, as well as regions of phytoplankton primary production. These features appear to be correlated with satellite observations from the coastal zone color scanner also on the Nimbus-7 satellite. Conspicuous coastal water features include plumes of decreased reflectivity, relative to the surrounding clearer water, which may be due either to phytoplankton blooms or, at the mouths of rivers (e.g., the Amazon and Congo rivers; see Plate 1), to UV-absorbing organic river effluents, including humic and fulvic acids [*Bukata et al.*, 1995].

Over land, prominent features with greater LER than average are associated with permanent glaciers, high desert (e.g., the Libyan desert), and regions with large dry lake and stream beds (e.g., Lake Eyre, Australia, and the Tibetan Plateau). Some of these same regions are also the sources of much of the desert dust seen blowing across Africa and the Atlantic Ocean [*Herman et al.*, 1997]. Relatively low reflectivities (0–2%) over land tend to be associated with moderate-elevation, vegetated regions, for example, the Pampas of Argentina and the central African highlands of southern Zaire and northern Zambia, eastern South Africa, and the western foothills of the Great Dividing Range of Australia. The low reflectivity observed over land is in agreement with recent measurements of vegetation-covered ground reflectivities obtained by *McKenzie et al.* [1996] in New Zealand.

On the basis of the ESLER and MLER maps the TOMS reflectivity data can distinguish at least six distinct surface-scene types: (1) light vegetation, (2) heavy vegetation, (3) high desert areas, (4) snow/ice and clouds, (5) clear water, and (6) water with plankton and silt, as well as seasonally persistent atmospheric clouds. The different scene types seen in the TOMS data for both land and water are independently seen in other ground-based and satellite data. The surface reflectivity data described in this paper can be obtained from the authors or from our anonymous ftp site (ftp://jwocky.gsfc.nasa.gov/pub/surface_reflectivity).

References

Bhartia, P. K., J. Herman, R. D. McPeters, and O. Torres, Effect of Mount Pinatubo aerosols on total ozone measurements from backscatter ultraviolet (BUV) experiments, *J. Geophys. Res.*, *98*, 18,547–18,554, 1993.

Bukata, R. P., J. H. Jerome, K. Y. Kondratyev, and D. V. Pozdnyakov, *Optical Properties and Remote Sensing of Inland and Coastal Waters*, CRC Press, Boca Raton, Fla., 1995.

Davé, J. V., Effect of aerosols on the estimation of total ozone in an atmospheric column from the measurement of its ultraviolet radiance, *J. Atmos. Sci.*, *35*, 899–911, 1978.

Diffey, B. L., A. T. Green, M. J. Loftus, G. J. Johnston, and P. S. Lee, A portable instrument for measuring ground reflectance in the ultraviolet, *Photochem. Photobiol.*, *61*, 68–70, 1995.

Doda, D. D., and A. E. S. Green, Surface reflectance measurements in the UV from an airborne platform, Part 1, *Appl. Opt.*, *19*, 2140, 1980.

Eck, T. F., and D. G. Dye, Satellite estimation of incident photosynthetically active radiation using ultraviolet reflectance, *Remote Sens. Environ.*, *38*, 135–146, 1991.

Eck, T. F., P. K. Bhartia, P. H. Hwang, and L. L. Stowe, Reflectivity of the Earth's surface and clouds in ultraviolet from satellite observations, *J. Geophys. Res.*, *92*, 4287–4296, 1987.

Eck, T. F., P. K. Bhartia, and J. B. Kerr, Satellite estimation of spectral UVB irradiance using TOMS-derived ozone and reflectivity, *Geophys. Res. Lett.*, *22*, 611–614, 1995.

Esaias, W. E., G. C. Feldman, C. R. McClain, and J. A. Elrod, Monthly satellite-derived phytoplankton pigment distribution for the North Atlantic Ocean basin, *Eos Trans. AGU*, *67*, 835, 1986.

Gordon, H. R., and M. M. Jacobs, Albedo of the ocean-atmosphere system: Influence of sea foam, *Appl. Opt.*, *16*, 2257, 1977.

Heath, D. F., A. J. Krueger, H. R. Roeder, and B. D. Henderson, The Solar Backscatter Ultraviolet and Total Ozone Mapping Spectrometer (SBUV/TOMS) for Nimbus G, *Opt. Eng.*, *14*, 323–331, 1975.

Henderson-Sellers, A., and M. F. Wilson, Surface albedo data for climatic modeling, *Rev. Geophys.*, *21*, 1743–1778, 1983a.

Henderson-Sellers, A., and M. F. Wilson, Albedo observations of the Earth's surface for climate research, *Philos. Trans. R. Soc. London, Ser. A*, *309*, 285–294, 1983b.

Herman, J. R., and D. Larko, Low ozone amounts during 1992–1993 from Nimbus-7 and Meteor-3 total ozone mapping spectrometer, *J. Geophys. Res.*, *99*, 3483–3496, 1994.

Herman, J. R., R. Hudson, R. McPeters, R. Stolarski, Z. Ahmad, X.-Y. Gu, S. Taylor, and C. Wellemeyer, A new self-calibration method applied to TOMS/SBUV backscattered ultraviolet data to determine long-term global ozone change, *J. Geophys. Res.*, *96*, 7531–7545, 1991.

Herman, J. R., R. McPeters, and D. Larko, Ozone depletion at northern and southern latitudes derived from January 1979 to December 1991 total ozone mapping spectrometer data, *J. Geophys. Res.*, *98*, 12,783–12,793, 1993.

Herman, J. R., P. K. Bhartia, J. Ziemke, Z. Ahmad, and D. Larko, UV-B increases (1979–1992) from decreases in total ozone, *Geophys. Res. Lett.*, *23*, 2117–2120, 1996.

Herman, J. R., P. K. Bhartia, O. Torres, C. Hsu, C. Seftor, and E. Celarier, Global distribution of UV-absorbing aerosols from Nimbus-7/TOMS data, *J. Geophys. Res.*, *102*, 16,911–16,922, 1997.

Hovis, W. A., et al., Nimbus-7 coastal zone color scanner: System description and initial imagery, *Science*, *210*, 60, 1980.

Hsu, N. C., J. R. Herman, P. K. Bhartia, C. J. Seftor, O. Torres, A. M. Thompson, J. F. Gleason, T. F. Eck, and B. N. Holben, Detection of biomass burning smoke from TOMS measurements, *Geophys. Res. Lett.*, *23*, 745–748, 1996.

Jaross, G., A. Krueger, R. P. Cebula, C. Seftor, U. Hartmann, R. Haring, and D. Burchfield, Calibration and post-launch performance of the Meteor-3/TOMS instrument, *J. Geophys. Res.*, *100*, 2985–2995, 1995.

Krueger, A. J., and M. R. Schoeberl, TOMS observations of total ozone in the 1986 Arctic spring, *Geophys. Res. Lett.*, *14*, 527–530, 1987.

Krueger, A. J., L. S. Walter, P. K. Bhartia, C. C. Schnetzler, N. A. Krotkov, I. Sprod, and G. J. S. Bluth, Volcanic sulfur dioxide measurements from the total ozone mapping spectrometer instruments, *J. Geophys. Res.*, *100*, 14,057–14,076, 1995.

Leffell, D. J., and D. E. Brash, Sunlight and skin cancer, *Sci. Am.*, *275*(1), 52–59, 1996.

Lenoble, J., *Atmospheric Radiative Transfer*, A. Deepak, Hampton, Va., 1993.

McClain, C. R., G. Feldman, and W. Esaias, Biological oceanic productivity, in *The Atlas of Satellite Observations Related to Global Change*, edited by R. Gurney, J. L. Foster, and C. L. Parkinson, pp. 251–263, Cambridge Univ. Press, New York, 1993.

McKenzie, R. L., M. Kotkamp, and W. Ireland, Upwelling UV spectral irradiances and surface albedo measurements at Lauder, New Zealand, *Geophys. Res. Lett.*, *23*, 1757–1760, 1996.

Morel, A., and A. Bricaud, Theoretical results concerning light absorp-

tion in a discrete medium, and application to specific absorption of phytoplankton, *Deep Sea Res., Part A*, *28*(11), 1375, 1981.

Schlesinger, B. M., and R. P. Cebula, Solar variation 1979–1987 estimated from an empirical model for changes with time in the sensitivity of the solar backscatter ultraviolet instrument, *J. Geophys. Res.*, *97*, 10,119–10,134, 1992.

Shifrin, K. S., *Physical Optics of Ocean Water* (translation of *Vvedenia v optiku morya* by D. Oliver), *AIP Transl. Ser.*, Am. Inst. of Phys., New York, 1988.

Tevini, M. (Ed.), UV-B radiation and ozone depletion: Effects on humans, animals, plants, microorganisms, and materials, A. F. Lewis, New York, 1993.

Wellemeyer, C. G., S. L. Taylor, G. Jaross, M. T. DeLand, C. J. Seftor, G. Labow, T. J. Swissler, and R. P. Cebula, Final report on Nimbus-7 TOMS Version 7 calibration, *NASA Contract. Rep.*, *4717*, 1996.

E. A. Celarier, Software Corporation of America, 4601 Presidents Suite 350, Lanham, MD 20706. (e-mail: edward.a.celarier.1@gsfc.nasa.gov)

J. R. Herman, Laboratory for Atmospheres, NASA Goddard Space Flight Center, Code 916, Greenbelt, MD 20771. (e-mail: herman@tparty.gsfc.nasa.gov)

(Received March 26, 1997; revised July 9, 1997;
accepted July 21, 1997.)